Visualization of liquid Helium flows generated by an oscillating rectangular cylinder

Patrik Švančara

Department of Low Temperature Physics
Faculty od Mathematics and Physics, Charles University in Prague
V Holešovičkách 2, 180 00 Prague 8, Czech Republic

Abstract

For the first time, a cylinder of rectangular cross section, performing quasi-harmonic oscillations in liquid helium, was employed for the experimental study of the dynamics of macroscopic vortex structures shed at the sharp edges of the obstacle. The flow of liquid helium was visualized by the motions of small, solidified deuterium particles, dispersed in the experimental cell and illuminated by a thin laser sheet. The particle positions were captured by a camera and the videos were processed in order to obtain their trajectories and velocities. A new scalar quantity was defined to properly characterize the magnitude of macroscopic vortices, both in He I, a classical viscous fluid, and He II, a fluid displaying superfluidity. We show that, at lower values of the relevant Reynolds number, the flows in He I and He II display a significant quantitative difference. This effect can be assigned to different length scales that limit coherent vortical structures in He I and He II. At large Reynolds numbers, the flows appeared instead to be similar, which agrees with the current understanding of quantum flows, at large enough length scales.

We acknowledge that this work represents a modified version of the bachelor thesis of the author, submitted at the Faculty of Mathematics and Physics, Charles University in Prague. Additionally, the results were published [1] and presented in both domestic and foreign conferences.

Keywords

low temperature physics • superfluidity • quantum turbulence • fluid mechanics

Preface

The liquefaction of helium, one of the most important milestones in low temperature physics, dates back to 1908. In Leiden, the Netherlands, the Dutch physicist Heike Kammerlingh Onnes obtained liquid helium at $4.2\,\mathrm{K}$, at the saturated vapor pressure. For his pioneering work Onnes was awarded the Nobel Prize in Physics in 1913.

Liquid ^{4}He exists in two phases: the normal phase, called He I, and the superfluid phase, known as He II. The latter occurs below $T_\lambda \approx 2.17\,\mathrm{K}$, at the saturated vapor pressure. The corresponding second order phase transition is called the λ transition (due to the shape of the specific heat curve in the proximity of T_λ) [2].

He I behaves as a classical viscous fluid with unusually low kinematic viscosity ($\nu \approx 2.5 \times 10^{-8}\,\mathrm{m^2 \cdot s^{-1}}$ at $3\,\mathrm{K}$ [3]) and its behavior is well described by the Navier-Stokes equation. On the other hand, He II sometimes behaves as an inviscid fluid. Furthermore, in He II one can observe a set of properties called superfluidity that result in the occurence of interesting phenomena, such as thermal counterflow, i.e., a thermally driven flow, the fountain effect, waves of temperature (called second sound) or quantum turbulence.

The phenomenological description of He II, named the two-fluid model, was developed by Tisza and Landau. In this model, it is assumed that the fluid is composed by the normal, viscous component, and the inviscid, superfluid component.

A different approach includes the quantum description of the superfluid component, which implies the existence of quantized vortices that are linear singularities, of ångstrom size, embedded in the superfluid. The circulation of the vortices is singly quantized, with quantum of circulation [2] $\kappa = 9.997 \times 10^{-8}\,\mathrm{m^2 \cdot s^{-1}}$. The motion of quantized vortices is very complex, including the formation of bundles and tangles of vortex lines. In special cases, the motion of quantized vortices can

produce quantum turbulence [4].

Thus, in order to fullfill the description of He II flows, we need to consider, beside the motion of the superfluid, the flow of the normal component as well as the interaction between these flow fields: therefore, a complete theoretical description is very difficult and yet lacking [4].

A poweful tool to study He II flows consists in performing experiments. Various experimental techniques were developed to date. One among them – visualisation – is based on the direct observation of the flow using, for example, small particles made of solidified hydrogen or deuterium, which are illuminated by a thin laser sheet [5]. One can observe that the motion of the particles is influenced by the flow and therefore one can infer the behavior of the flow itself.

A cylinder of rectangular cross-section was used to generate the flow in the liquid. It performed quasi-harmonic oscillations in the vertical direction. A wide range of Reynolds numbers was obtained, at different temperatures, both in He I and He II. The motion of particles was captured by a digital camera.

Raw results from the camera were processed using the particle tracking velocimetry (PTV) technique that is based on the detection of particle trajectories and their development in time, providing thus the velocity or acceleration of the particles.

The aim of the performed experiment was to observe, for the first time, the behavior of the macroscopic vortex structures, if any, shed by the sharp edges of the moving cylinder, in He I and He II, and report their qualitative and quantitative characteristics, as the properties of large vortex structures in He II are yet to be fully understood.

Besides, the comparison between the results obtained in He II and in a classical viscous fluid, i.e., He I, under similar conditions, can give further insight into the similarities and differences between viscous and quantum flows and provide consequently new information about the dynamics of quantum flows.

1   Theoretical Part

1.1   Properties of Helium at Low Temperatures

Two stable isotopes of He can be found in nature: the less abundant ^{3}He, whose nucleus is composed of two protons and a neutron, and the more common ^{4}He, whose nucleus, called the α particle, is made of two protons and two neutrons. The resulting spin of the nucleus implies that ^{3}He is a fermion, which follows the Fermi-Dirac statistics, whereas ^{4}He is a boson, so it follows the Bose-Einstein distribution. This fact leads to significant differences in the low temperature limit. In this work we will be concerned exclusively with the low temperature properties of ^{4}He.

Two orbiting electrons form a closed s orbital and this implies that helium belongs to the group of noble gasses in the Mendeleev table of elements. The only interaction between He atoms is the van der Waals force. Compared to other chemical bounds, this interaction is considered weak. As a consequence, helium gas at room temperature acts almost as an ideal monoatomic gas.

Equilibrium Phase Diagram of ^{4}He

^{4}He can be found in multiple phases. Its phase diagram, however, differs from that of most known substances (see fig. 1.1). The critical point of ^{4}He is located at $T_{\mathrm{C}} \approx 5.2\,\mathrm{K}$ and $p_{\mathrm{C}} \approx 226\,\mathrm{kPa}$ [2]. Following the saturated vapor pressure curve, one, however, never reaches the triple point, i.e., the point of the coexistence of solid, liquid and gaseous phases.

This fact means that at low pressures ^{4}He stays in the liquid state even in the absolute zero limit. The solid ^{4}He phase occurs only at pressures greater than approximately $2.5\,\mathrm{MPa}$.
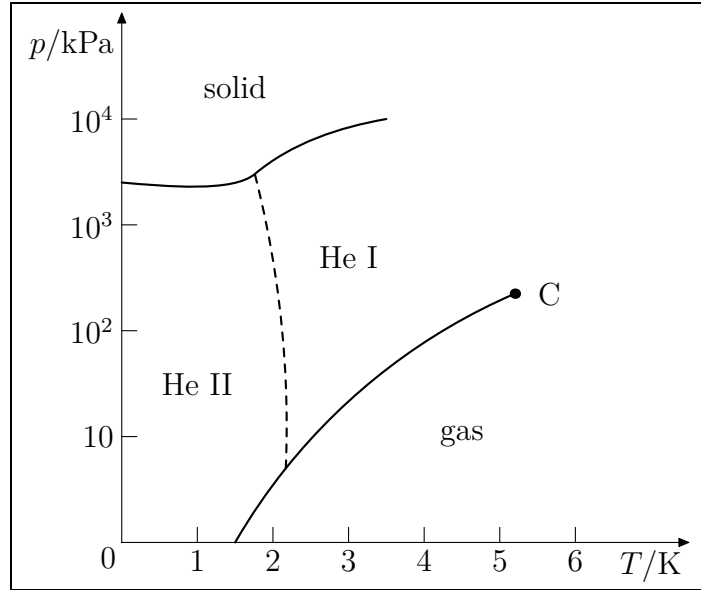
Figure 1.1: Equilibrium phase diagram of ^{4}He. The dashed line represents the λ line, i.e., the line of the lambda transition. The point C is the critical point.

The Lambda Transition and Superfluidity

In addition, liquid helium undergoes a second order phase transition, called the lambda transition, see fig. 1.1. The temperature of the lambda transition, at the saturated vapor pressure, is $T_\lambda \approx 2.17\,\mathrm{K}$. Its name is derived from the shape of the specific heat curve of the liquid in the proximity of T_λ. Liquid above this temperature is called He I, whereas liquid below T_λ is named He II.

The first experiments studying the lambda transition detected significant differences between He I and He II. For instance, the heat conductivity of liquid He II is up to 10^6 times larger than that of He I [3], and some hydromechanical properties change dramatically. It was observed that He II, under different conditions, behaves as inviscid or viscous fluid.

Kapitsa [6] showed that He II can easily flow through narrow channels, appearing to have no internal friction, known as viscosity. Kapitsa named this phenomenon "superfluidity", because of the analogy with superconductivity, that can be understood as the superflow of electrons in the crystal lattice of metals.

Allen and Jones [7] discovered that, in He II, the temperature and pressure gradients are linked together. The change of pressure due to the change of temperature is called the fountain effect, while the reverse effect is known as the mechano-caloric effect.
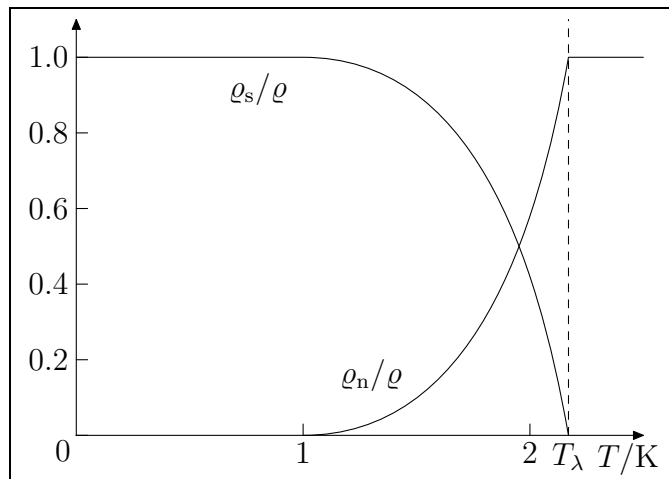
1.2   The Two-fluid Model

In 1938 Tisza postulated [8] that He II is composed of two liquids, the viscous phase and the inviscid phase. His theory, based on an idea of London, explained earlier experimental results. The origin of the superfluidity was supposed to be the Bose-Einstein condensation of the helium atoms.

However, the work of Tisza and London was criticised by Landau, who provided another theory of superfluidity [9]. In his theory, the gas of non-interacting quasiparticles, phonons and rotons, represented the elementary excitations of the liquid.

Landau's theory also suggests, that, from the phenomenological point of view, He II can be understood as a mixture of two phases: the normal phase, representing the quasiparticles, and the superfluid phase. The normal phase is responsible for the viscosity and carries the entire entropy S of the liquid.

The densities of the normal, ϱ_n, and superfluid, ϱ_s, phases are strongly temperature dependent. However, the total He II density, $\varrho = \varrho_n + \varrho_s$, varies only weakly with temperature. Therefore, the ratio of the normal to superfluid components change with respect to the temperature of the liquid (see fig. 1.2).

Figure 1.2: The temperature dependence of the densities of the normal (ϱ_n) and superfluid (ϱ_s) components, as described in the two-fluid model.

This dependence was first observed experimentally by Andronikashvili [10]. A set of thin disks was used to make a torsion pendulum. This pendulum, submerged in He II, appeared to have a different period of oscillations compared to that in a vacuum chamber. This means that the effective mass (and the moment of

inertia) was greater in He II than in vacuum, because the viscous normal phase was dragged with the moving disks. From these results Andronikashvili was able to state the ratio of the normal and superfluid phases at various temperatures, see fig. 1.2 again.

1.3   Hydromechanical Equations for He II

As mentioned above, the two-fluid theory suggests that He II can be understood as a mixture of the normal and superfluid components. Therefore, we must consider two velocity fields: $\mathbf{v}_n$, for the normal component, and $\mathbf{v}_s$, for the superfluid component.

When the flow is driven mechanically, it is assumed that both components move in the same direction, i.e., $\mathbf{v}_n \approx \mathbf{v}_s$, and we talk about *coflow*. However, when the liquid is forced to flow through a narrow capillary or a porous material, the normal component is slowed down due to its finite viscosity, whereas the superfluid component can flow through it. The flow of the pure superfluid is called *superflow*. Finally, the last type of flow – thermal *counterflow* – occurs when the phases of He II flow in opposite directions [4].

In order to fullfill mathematically such a description, one must write two Navier-Stokes equations for both components. Assuming that the flow is incompressible, i.e. $\nabla \cdot (\mathbf{v}_n + \mathbf{v}_s) = 0$, we get [11] for the superfluid component,

$$\varrho_s \frac{\partial \mathbf{v}_s}{\partial t} + \varrho_s(\mathbf{v}_s \cdot \nabla)\mathbf{v}_s = -\frac{\varrho_s}{\varrho}\nabla p + \varrho_s S\nabla T + \frac{\varrho_n \varrho_s}{2\varrho}\nabla\left(\mathbf{v}_n - \mathbf{v}_s\right)^2 - \mathbf{F}_{ns}, \quad (1.1)$$

and for the normal component,

$$\varrho_n \frac{\partial \mathbf{v}_n}{\partial t} + \varrho_n(\mathbf{v}_n \cdot \nabla)\mathbf{v}_n = -\frac{\varrho_n}{\varrho}\nabla p - \varrho_s S\nabla T - \frac{\varrho_n \varrho_s}{2\varrho}\nabla\left(\mathbf{v}_n - \mathbf{v}_s\right)^2 + \mathbf{F}_{ns} + \eta\nabla^2\mathbf{v}_n. \quad (1.2)$$

The third term on the right hand side of equation (1.1) describes the interaction related to the counterflow, the fourth term of the same equation represents the mutual friction force.[1] This force can be understood as the scattering of phonons and rotons, i.e., the quasiparticles of elementary excitations that represent the normal component, on the quantized vortex cores (see below). The mutual friction thus describes the interaction between the components.

_____

[1]Note that the same terms, but with opposite signs, appear also in equation (1.2).

For the sake of completeness, one must consider the conservation of mass law as well:

$$\frac{\partial \varrho}{\partial t} + \nabla \cdot (\varrho_s \mathbf{v}_s + \varrho_n \mathbf{v}_n) = 0\,. \tag{1.3}$$

Let us assume the simplest case of the flow: beside incompressible flow, we will consider isothermic flow ($\nabla T = 0$) and the absence of counterflow ($\mathbf{v}_n - \mathbf{v}_s = 0$). Assuming zero mutual friction force in addition, we arrive to the simple, well known form of the equations:

$$\varrho_s \frac{\partial \mathbf{v}_s}{\partial t} + \varrho_s (\mathbf{v}_s \cdot \nabla) \mathbf{v}_s = -\frac{\varrho_s}{\varrho} \nabla p\,, \tag{1.4}$$

and

$$\varrho_n \frac{\partial \mathbf{v}_n}{\partial t} + \varrho_n (\mathbf{v}_n \cdot \nabla) \mathbf{v}_n = -\frac{\varrho_n}{\varrho} \nabla p + \eta \nabla^2 \mathbf{v}_n\,. \tag{1.5}$$

The first equation is the Euler equation for an incompressible ideal fluid, the second one is the Navier-Stokes equation for an incompressible Newtonian fluid. Therefore, the two-fluid model can be considered as a complex approach to the overall beahvior of He II, which includes, e.g., the mechano-caloric effect, the existence of counterflow and the mutual friction force. These effects, however, cannot be understood using the classical approach and they require the quantum description of the superfluid phase.

1.4   Quantum Behavior of He II

London suggested, in order to describe the frictionless flow of the superfluid component, to define the macroscopic wave function $\psi(\mathbf{r}, t)$, a complex function of real coordinates and time. Following a quantum mechanics point of view, the squared modulus $|\psi|^2$ must give us the number of ^{4}He atoms in the superfluid state, i.e.,

$$\psi^*(\mathbf{r}, t)\, \psi(\mathbf{r}, t) = |\psi|^2 = \varrho_s / m_4, \tag{1.6}$$

where m_4 is the mass of the ^{4}He atom.

Let us assume that one can write the wave funcion in the form

$$\psi(\mathbf{r}, t) = \psi_0\, \mathrm{e}^{i\phi(r,t)}, \tag{1.7}$$

where ψ_0 is the amplitude and ϕ indicates the phase of the wave function. Applying the condition (1.6), we get for the amplitude $\psi_0 = \sqrt{\varrho_s/m_4}$, as the squared modulus of a complex exponential is always equal to 1.

If we apply the momentum operator $\hat{\mathbf{p}}$ to (1.7), we get

$$\hat{\mathbf{p}}\psi = -i\hbar\nabla\left(\psi_0\,\mathrm{e}^{i\phi(r,t)}\right) = \hbar\psi_0\nabla\left(\mathrm{e}^{i\phi(r,t)}\right) = \hbar\nabla\phi(r,t)\psi. \qquad (1.8)$$

Therefore, the eigenvalue of the momentum operator is $\mathbf{p} = \hbar\nabla\phi$. As this value is related to the motion of ^{4}He atoms, we can write

$$\mathbf{v}_s = \frac{\mathbf{p}}{m_4} = \frac{\hbar}{m_4}\nabla\phi. \qquad (1.9)$$

The velocity field of the superfluid component is given as a gradient of the scalar funcion ϕ, so the flow is *potential*. Therefore, the flow automatically satifies the zero vorticity condition, $\boldsymbol{\omega} = \nabla \times \mathbf{v}_s = 0$, in a simply connected fluid region.

Quantized Vortices

The circulation Γ of a liquid is defined as a closed path integral

$$\Gamma = \oint_{\mathfrak{L}} \mathbf{v}_s \cdot \mathrm{d}\boldsymbol{\ell} = \frac{\hbar}{m_4} \oint_{\mathfrak{L}} \nabla\phi \cdot \mathrm{d}\boldsymbol{\ell}, \qquad (1.10)$$

where $\mathfrak{L}$ is a closed curve in the volume and $\mathrm{d}\boldsymbol{\ell}$ a vector tangent to a short portion of $\mathfrak{L}$. As the wave function must be well-defined in every point, the phase ϕ may differ only by any multiple of 2π along any enclosed curve.
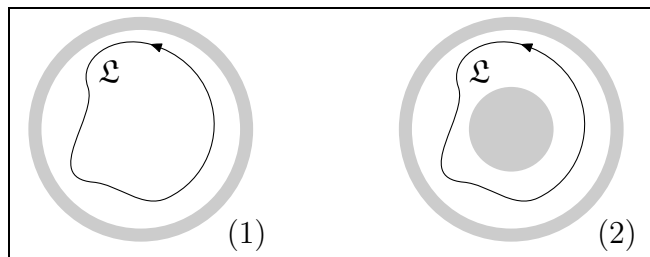
Figure 1.3: Schemes of (1) a simply connected domain and (2) a multiply connected domain.

Consider two regions of interest, shown in fig. 1.3. Region (1) represents a simply connected domain in an He II volume, region (2) is multiply connected. In the first case, the curve $\mathfrak{L}$ can be shortened to a simple point. Therefore, the phase

function ϕ must not differ by any multiple of 2π and the closed integral (1.10) yields $\Gamma_{(1)} = 0$.

However, in the second case, the topology of the considered space allows the phase ϕ to differ by a factor $2\pi n$, where n is an integer. As a consequence, the circulation is nonzero and equal to

$$\Gamma_{(2)} = \frac{\hbar}{m_4} 2\pi n = n\frac{h}{m_4} = n\kappa, \tag{1.11}$$

which means that the circulation in the superfluid is quantized, with the *quantum of circulation* $\kappa = h/m_4 = 9.997 \times 10^{-8}\,\mathrm{m^2 \cdot s^{-1}}$ [2].

Surprisingly, multiply connected domains exist naturally in He II. They are known to be the linear singularities of the wave funcion and are called the vortex cores or quantized vortex lines. They have a diameter of the order of a few ångstroms, but their length is usually macroscopic. According to the Kelvin theorem, vortex cores can end at the surface of the container or at the surface of the liquid, or, alternatively, form a closed curve, called *vortex ring*.

The profile of the tangential velocity (that is the only one relevant for the value of Γ) of the superfluid component $v_s^\perp(r)$, where r denotes the radial distance from the vortex core, in the idealized case of a single vortex line in an infinite tank, is

$$v_s^\perp(r) = \frac{\kappa n}{2\pi r}, \tag{1.12}$$

which satisfies the condition $\Gamma = \kappa n$ around any closed contour $\mathfrak{L}$. Note that the infinite value of $v_s^\perp$ at $r \to 0$ is compensated by the zero density of the superfluid component in the centre of the vortex.

Additionally, the energy per unit length of this vortex, with core radius a, placed in a container of radius b, can be written as

$$E_n = \int_a^b \frac{1}{2}\varrho_s v_s{}^2\,\mathrm{d}S = \int_a^b \varrho_s v_s{}^2\pi r\,\mathrm{d}r = \frac{\varrho_s\kappa^2}{4\pi}n^2\int_a^b \frac{\mathrm{d}r}{r} = \frac{\varrho_s\kappa^2}{4\pi}n^2\ln\left(\frac{b}{a}\right). \tag{1.13}$$

As the energy is proportional to n^2, the formation of a quantized vortex with $n = 2$ consumes 2-times more energy than the formation of two individual vortices. Therefore, as the principle of the lowest energy dictates, quantized vortices always decay to the singly quantized state.

1.5   Oscillatory Motion in He II

The phenomenon of turbulence is, even nowadays, a yet not completely understood problem of classical physics. Current research tries to investigate the formation of vortices and their development in time. Classical theory suggests that the energy in turbulent flows is, firstly, transferred, via the Richardson cascade, from bigger to smaller vortices. Then, at the Kolmogorov length, the energy is dissipated into heat due to the nonzero fluid viscosity [2, 12].

Instead, quantum turbulence can be understood as the dynamic motion of the tangle of vortex lines occuring in superfluids such as He II. It can be driven mechanically, e.g., using a moving body submerged in the liquid, or thermally in the counterflow regime. In the zero temperature limit, when the amount of the normal component in He II is negligible, quantum turbulence occuring in a pure superfluid represents a simpler, quantized, type of turbulence, compared to its classical counterpart.

However, at length scales larger than or of the same order of the mean intervortex distance, the quantized nature of quantum turbulence vanishes. Hence, the turbulent flow displays a statistical similarity with its classical analogue [12, 13].

Therefore, the harmonic motion of a macroscopic obstacle in He II can be described with the mathematical apparatus of classical hydrodynamics. For the simplest case, i.e., an oscillating cylinder, the flow can be characterized with two dimensionless parameters [14]: the Stokes number

$$\beta = \frac{\omega d^2}{2\pi\nu}, \tag{1.14}$$

and the Keulegan-Carpenter number

$$\mathrm{KC} = \frac{2\pi a}{d}, \tag{1.15}$$

where a is the amplitude of the oscillatory motion with angular frequency ω; d denotes the characteristic dimension of the oscillating body and ν stands for the kinematic viscosity of the fluid. These two parameters, combined together, give the Reynlods number

$$\beta \cdot \mathrm{KC} = \frac{a\omega d}{\nu} = \mathrm{Re}. \tag{1.16}$$

However, note that this approach may not be valid anymore at length scales

where the quantized nature of turbulence in He II is not negligible.

Since the Keulegan and Carpenter paper [14], a number of experiments studying the flow past a round obstacle were performed – mostly in normal liquids. Only a few expriments were concerned with the flow in superfluid liquids. However, these experiments already detected distinct differences between classical and quantum flows, see, e.g., [5, 15, 16] and references therein.

Alternatively, the use of sharp-edged oscillating bodies can provide additional information on the issue of shed vortices. For example, the flow induced by the motion of a flat disc in a viscous fluid was studied by Tao and Thiagarajan [17]. They observed three regimes of the vortex formation, depending mostly on the thickness to diameter ratio of the disk. This means that, for sharp-edged bodies, the flow described only by β and KC cannot be directly compared with results obtained for a circular cylinder, as those parameters do not bring enough information about the flow conditions.

Hence, the flow induced by sharp-edged bodies is qualitatively different from the better-examined flow around round bodies. So, special care should be taken to describe the flow conditions to its full extent. In addition, the same oscillating object may generate different flow patterns in a classical fluid, such as He I and a superfluid, such as He II. However, the research on these specific flow conditions is yet in its infancy.

Experimental Techniques

Two experimental approaches are being currently used to study oscillatory motions in superfluid He. The first one employs small oscillators, such as the widely used quartz tuning forks (see fig. 1.4). The forks usually oscillate at high frequencies (of the order of 10^4 Hz) and with adjustable amplitude. The flow of the fluid is difficult to visualise, so the fork itself is used as a probe: the flow characteristics are evaluated from the measurement of the resonance frequency shift of the fork. It was observed [15], that the forks can induce both laminar and turbulent flow regimes, in He I and in He II as well.

The second, relatively new, type is based on the oscillatory motion of a solid body in the liquid helium bath. The body, of size of a few milimeters, oscillates at a frequency of the order of 1 Hz. This method allows the use of various visualisation techniques, such as particle tracking velocimetry, as the flow in the proximity of

the body is slow enough.

The harmonic motion of the body leads to the repeated generation in the fluid of vortices of similar size and position, providing the opportunity of the statistical study of large vortex structures.
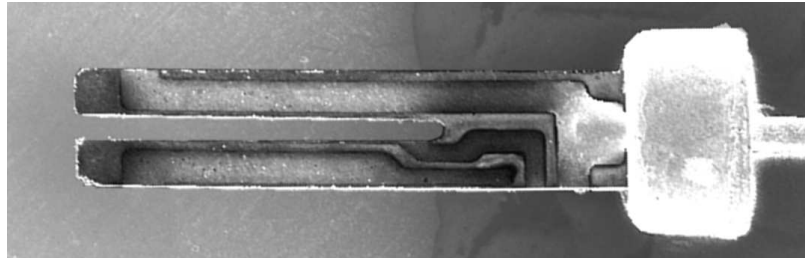
Figure 1.4: Microphotography of a tuning fork being used at Joint Low Temperature Laboratory in Prague. We are thankful to David Schmoranzer for providing the photography.

1.6   Questions to Be Answered

In this work, we discuss the flow generated by a sharp-edged body, i.e., a rectangular plexiglass cylinder. Preliminary observations showed that the vortices are often formed in the proximity of the sharp edges of the cylinder. We can assume that, in He II, the vortices are created in the coflow regime, meaning that both components move together.

However, the motion of the tangle of quantized vortex lines, shed by the moving body, must obey the laws of quantum mechanics and its own hydrodynamics, discussed above.

This fact arises many questions that are, for example, does the tangle of vortex lines influence the motion of the whole liquid in the proximity of an oscillating body? Does the flow generated by the cylinder in He II differ from the results reported in [17]? Does quantum turbulence influence the dynamics of big vortices? Our work aims to contribute to the clarification of these topics that are not yet well understood.

2   Experimental Setup

The study of liquid helium flows by visualisation techniques requires a setup that is made of various components. The experimental cell with liquid helium must be well-isolated from parasitic heat fluxes. However, at the same time, the cell must allow optical access to the experimental volume.

The method that was applied is called particle tracking velocimetry or PTV. It consist of tracking the positions of small particles, dispersed in the helium volume, with respect to time. The acquired data are then processed, in order to obtain quantitative characteristics of the flow.

2.1   Apparatus

A custom-made cryostat, i.e., an isolated vessel for cryogenic fluids, was designed in Prague and manufactured by Precision Cryogenic Systems (U.S.A.).

The inner volume of the cryostat can contain up to 40 liters of liquid helium. In order to minimize the parasitic heat input, two types of thermal isolation are in use: liquid nitrogen bath and vacuum cavities.

Besides the helium vessel, the cryostat is equipped with another volume of 35 liters that contains

Figure 2.1: Photgraph of the cryostat.

liquid nitrogen. As this vessel is in thermal contact with the inner helium bath, liquid nitrogen is used to pre-cool the walls of the cryostat. During the experiment, the nitrogen prevents the heat input due to radiation, as its temperature is, in our setup, about $77\,\mathrm{K}$.

Between the helium and nitrogen vessels, and the nitrogen vessel and the outer surface of the cryostat, there are two vacuum cavities, evacuated to pressures smaller than $0.1\,\mathrm{Pa}$. The aim of this isloation is to minimize the conductive heat transfer.

The optical tail is located at the bottom of the cryostat. It provides the optical access through five windows, each of $25\,\mathrm{mm}$ diameter. Every window is made of three glasses: the inner one is made of sapphire (as it reduces the heat input), the other two are quartz windows.
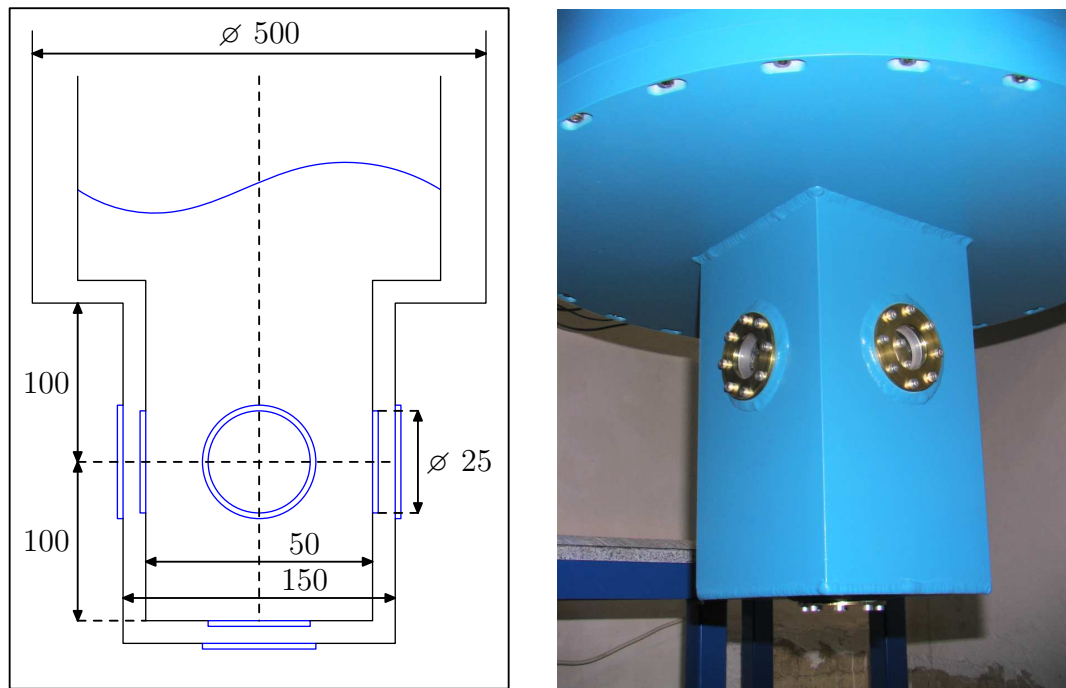
Figure 2.2: *Left:* Scheme of the experimental cell. Note that the scheme is not to scale, dimensions are in milimeters. For the sake of simplicity, the third layer of the cryostat wall is not included. *Right:* Photograph of the experimental cell.

Helium is transferred into the cryostat from a transport Dewar vessel at approximately $4\,\mathrm{K}$, at higher-than-atmospheric pressure. The overpressure ensures that no air would leak into the transfer container. Once liqud helium is in the cryostat, its vapors are pumped. As the pressure in the cryosatat is lower than the pressure of saturated vapors, the helium strongly evaporates, consuming the heat of evaporation. Therefore, the temperature of the liquid drops. If we assume that the pumping rate is slow enough, so that, at any time, the vapors above the liquid are

in the saturated state, one can easily obtain the temperature from the value of the pressure, as the relation between saturated vapor pressure and temperature is well-known and tabulated [3].

The pumping unit consist of two Pfeiffer pumps. The standard rotary pump (maximum flow rate of $324\,\mathrm{m^3{\cdot}h^{-1}}$) ensures the pumping from atmospheric pressure to the pressure of $10\,\mathrm{kPa}$. For smaller pressures the Root pump is added in series, resulting to the maximum flow rate of $36\,\mathrm{m^3{\cdot}h^{-1}}$. The pressure in the inner volume of the cryostat is measured by a Barotron gauge, with the sensitiviy of $0.1\,\mathrm{torr} \approx 13.3\,\mathrm{Pa}$.

The flow rate of the outcoming helium vapors is regulated via a computer driven butterfly VAT valve or by a manually operated bypass valve, which are both located above the pumping unit. In order to isolate the apparatus from the vibrations of the pumping unit, a custom-made T-piece and a long corrugated tube connect the cryostat to the butterfly valve.

In addition, two resistive thermometers are in use. The temperature dependence of their resistance is known from a previous calibration. Hence it is possible to obtain the temperature of the helium bath with great precision from their resistance. The latter can be calculated as the ratio of measured voltage and current using a standard four-terminal sensing.
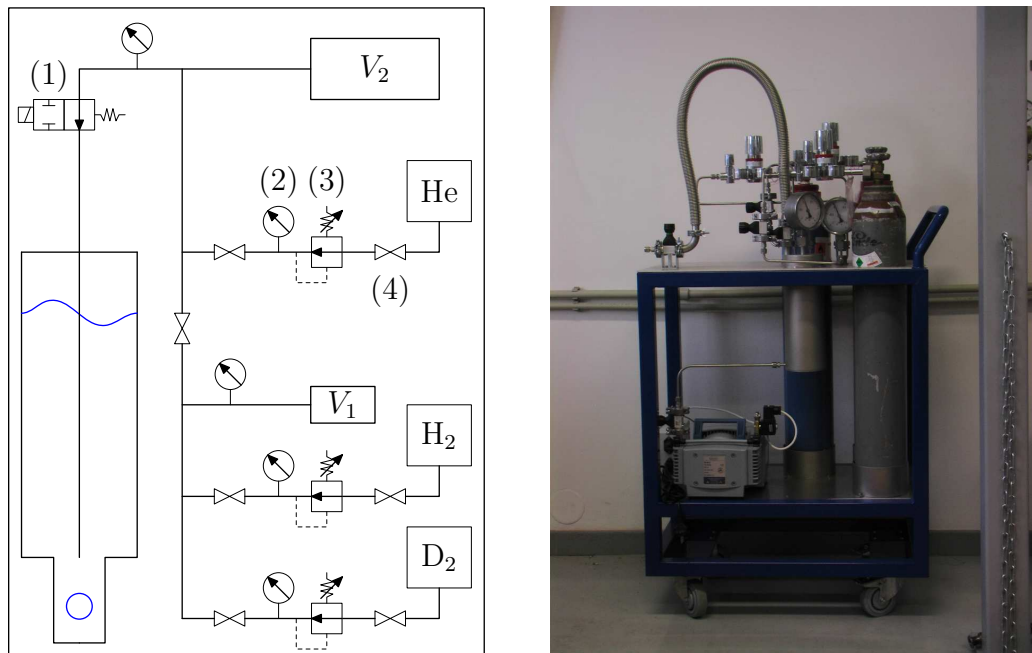
2.2 Seeding System

The key problem in flow visualisation experiments lies in the choice of suitable tracer particles. As the density of liquid helium is considerably small ($\varrho \approx 146\,\mathrm{kg{\cdot}m^{-3}}$ at $2\,\mathrm{K}$), all commonly used solid materials would sink, as their density is greater than ϱ.

It appears that small frozen particles of hydrogren (H_2) and deuterium (D_2) are the most suitable materials. Both can be found in the solid state at liquid helium temperatures (their melting temperatures are $14\,\mathrm{K}$ and $19\,\mathrm{K}$, for H_2 and D_2, respectively), and their densities are $\varrho_{H_2} = 88\,\mathrm{kg{\cdot}m^{-3}}$ and $\varrho_{D_2} = 200\,\mathrm{kg{\cdot}m^{-3}}$, for hydrogen and deuterium, respectively [18].

Therefore, the seeding system for hydrogen and/or deuterium particles was designed, see fig. 2.3. Hydrogen and/or deuterium are, at first, mixed in a small volume V_1, at room temperature. Then, the gas is transferred to the volume V_2,

that is approximately 50 times larger. At this point, gaseous [4]He is added. It was found [18] that the most suitable mixture is obtained when the amount of helium is approximately 100 times grater than the amount of hydrogen or deuterium. Finally, the mixture is injected in He I via a fast solenoid valve and, during the injection, the mixture solidifies, inside the seeding capillary, in the form of small particles.

Figure 2.3: *Left:* Scheme of the seeding system. (1) Solenoid valve, (2) pressure gauge, (3) pressure regulator, (4) valve. V_1 and V_2 denote mixing volumes, He, H_2 and D_2 represent high-pressure gas vessels. *Right:* Photograph of the seeding system.

If we compare the densities ϱ_{H_2} and ϱ_{D_2} with ϱ, we can conclude that the total force[1] acting on H_2 particles points upwards (particles tend to float), while the force acting on D_2 particles points downwards (particles sink).

The ideal tracer particles are such that the total force is zero, i.e., the density of the particles is equal to ϱ. It was expected that those particles may be formed from a suitable mixture of hydrogen and deuterium gas. However, it was found out [12] that the particles formed from the mixture are of two types: pure hydrogen and pure deuterium particles. As the melting temperatures of the isotopes are slightly different, the desublimation from gaseous to solid phase occurs firstly for deuterium and after for hydrogen.

Assuming a spherical shape for the small particles, the only forces acting on

---

[1]The total force is the vector sum of the gravity force and the buoyancy force.

a particle moving slowly in a classical fluid, such as He I, are the gravity, the buoyancy force and the Stokes drag force. After a sufficient amount of time, these forces are balanced, resulting into a uniform motion with a velocity v_{eq} that is dependent, besides physical constants, of the particle radius r only

$$v_{\text{eq}} = \frac{9\nu}{2(\varrho_{\text{p}}/\varrho - 1)gr^2},\tag{2.1}$$

where ν is the kinematic viscosity and ϱ the density of the liquid, ϱ_{p} indicates the particle density and g denotes the gravitational acceleration. Therefore, by measuring the velocities of the particles in a container of still liquid helium, one can establish their approximate radii [18]. However, keep in mind that the actual shape of the particles is not spherical.

In our setup, at $1.66\,\text{K}$ and $1.77\,\text{K}$, the radii of deuterium particles were found to be $(10 \pm 3)\,\mu\text{m}$ and $(5 \pm 2)\,\mu\text{m}$, respectively [12].

2.3   Oscillating Cylinder Design

The key component of our setup is an oscillating cylinder of rectangular cross section. It was made of transparent plexiglass (for the relevant dimensions see fig. 2.4) as it absorbs only a small fraction of the incident light power. It was observed [19] that, when a black metalic cylinder was used, the temperature increase due to the light absorption induced a measurable evidence of the presence of counterflow.

The cylinder was attached to a long metalic shaft in such a way that the walls of the cylinder were parallel to the walls of the optical tail of the cryostat.

A narrow, air-tight channel was made for the shaft to exit the inner volume of the cryostat. An overpressure of gaseous helium in this channel was ensured in order to isolate the inner volume of the cryostat from any air leakage.

Finally, the shaft was attached to a Maxon motor, type EC 32. The mechanism, composed of a disk and a crank, transferred the rotational motion of the motor to the periodic vertical motion of the shaft, see fig. 2.5.
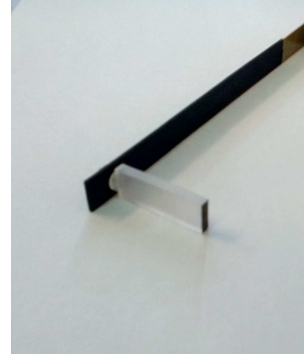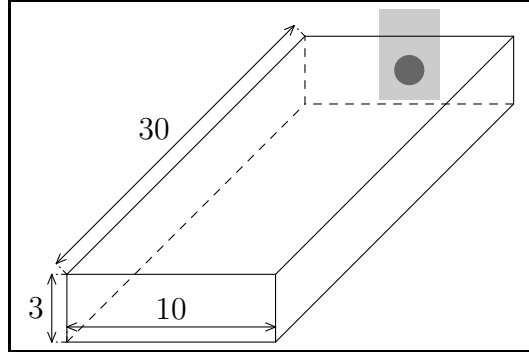
Figure 2.4: *Left:* Scheme of the plexiglass cylinder. Note that the scheme is not to scale. Dimensions are in milimeters. On the background wall of the cylinder, the bottom end of the shaft is shown. *Right:* Photograph of the cylinder attached to the shaft.
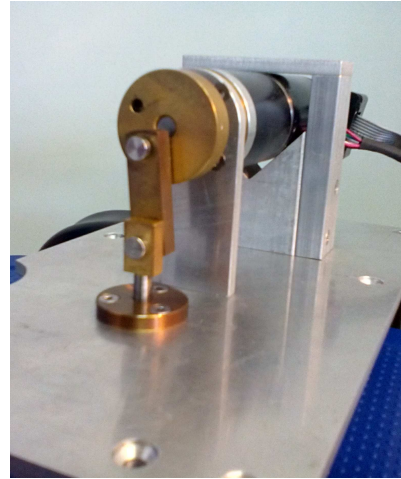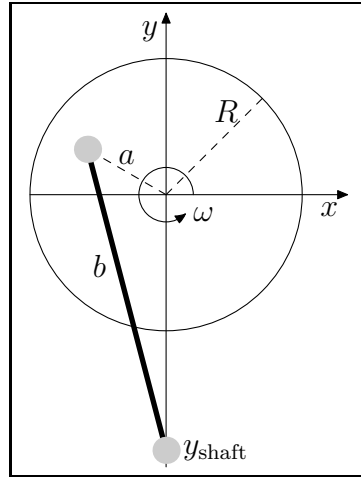

Figure 2.5: *Left:* Scheme of the upper end of the shaft attached to the motor. Disk radius $R = 15\,\text{mm}$, crank length $b = 25\,\text{mm}$, amplitude $a = 10\,\text{mm}$ (adjustable also to $5\,\text{mm}$). *Right:* Photograph of the mechanism attached to the motor.

Using elementary geometry, one can calculate the exact motion of the upper end of the shaft, with respect to the coordinate system shown in fig. 2.5:

$$y_{\text{shaft}}(t) = a\sin(\omega t) - \sqrt{b^2 - a^2\cos^2(\omega t)}. \tag{2.2}$$

The motion described by the equation above cannot be considered harmonic, as the formula cannot be, for any a and b, expressed as a simple sine or cosine function. However, if we compare the plot of the funcion above and the plot of an harmonic function, see fig. 2.6, we can conclude that the motion of the shaft is *quasiharmonic*, i.e., similar to the harmonic motion.

In our setup, the frequency of the motor ranged from $0.05\,\text{Hz}$ to $1.25\,\text{Hz}$. Besides,
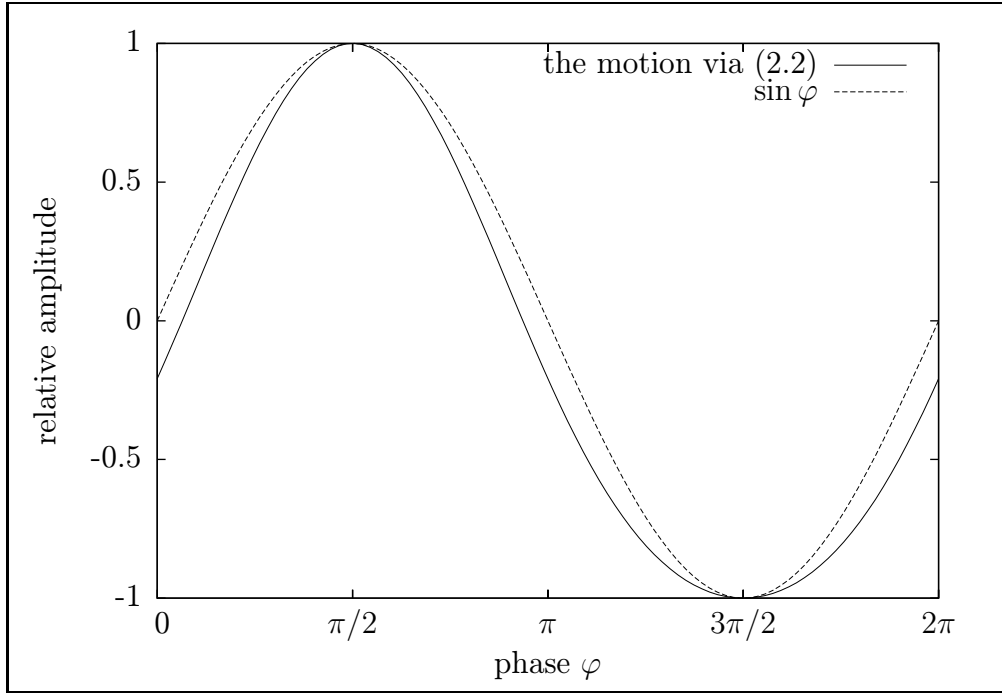
Figure 2.6: Plots of the function (2.2) and a harmonic sine function. Note that, in (2.2), the values were shifted and scaled in order to obtain $y_{\mathrm{shaft}}(\max) = 1$ (at $\varphi = \omega t = \pi/2$) and $y_{\mathrm{shaft}}(\min) = -1$ (at $\varphi = 3\pi/2$).

we used two different oscillation amplitudes, of $5\,\mathrm{mm}$ and $10\,\mathrm{mm}$, respectively.

2.4 Data Acquisition

The goal of our experimental setup was to obtain videos showing the motion of the particles dispersed in the experimental cell. For this purpose, a typical visualisation equipment was used: a thin plane inside the optically-accessible tail of the cryostat was illuminated by a laser sheet; then, the motion of the particles was captured by a camera; after that, the frame sequences were stored to be processed later.

Laser and Optics

The laser, RayPower 5000 by Dantec Dynamics, is a standard, continuous-wave solid-state laser, that emits green light ($\lambda = 532\,\mathrm{nm}$). The adjustable power of the laser can go up to $10\,\mathrm{W}$. However, for our purposes, the power did not exceed $0.2\,\mathrm{W}$.

The optical setup is composed of 3 lenses that disperse the laser beam into a sheet of about 10 mm high and 1 mm thick. The light sheet enters the inner volume of the optical tail in its middle and it is parallel to its walls.

Camera

We used a high-speed CMOS camera (Phantom v12), with maximum frame rate of ca. 6 000 fps, at 1 Mpix (1280 × 800 px) [18]. The camera was placed perpendicularly to the laser sheet and focused on the illuminated plane using a Canon 180 mm macro lens. The camera and the laser are controlled via Dynamic Studio, a software by Dantec Dynamics.

The physical size of one pixel, $20\,\mu\text{m} \times 20\,\mu\text{m}$, does not correspond to the physical size of the region captured by this pixel (i.e, the apparent pixel size). Therefore, a calibration was done. As the refractive index of liquid helium is approximately equal to 1, it is possible to perform the calibration when the cryostat is filled with air. Firstly, a ruler is put in the approximate middle of the experimental cell. Then, the camera is focused on the ruler in such a way it captures the ruler marks. After that, an operator marks a known distance in the captured frame and finally, a software routine calculates the scaling factor, i.e., the ratio between the apparent and the physical pixel size. For our setup, the scale factor was measured to be $s = 1.335$, which means that the distance of 1 cm is represented by 374 px.

Hence, the resolution of $1\,280 \times 800\,\text{px}$ represents a field of view of $34 \times 21\,\text{mm}^2$.

2.5   Data Processing

Raw data – videos of 2 000 frames at 100 fps, i.e., about 250 GB of data in total – were processed using the particle tracking velocimetry technique. For each frame the particles were detected and the obtained positions were subsequently linked in time, i.e., between frames, providing thus the temporal development of particles' trajectories. As the conditions of the video capturing (e.g., the total amount of particles or the phase shift of the cylinder at the beginning of the video) differ from run to run, a suitable set of parameters for the processing software had to be found manually for each video. Hence, besides various Excel and Matlab

routines, the work required a considerable amount of time.
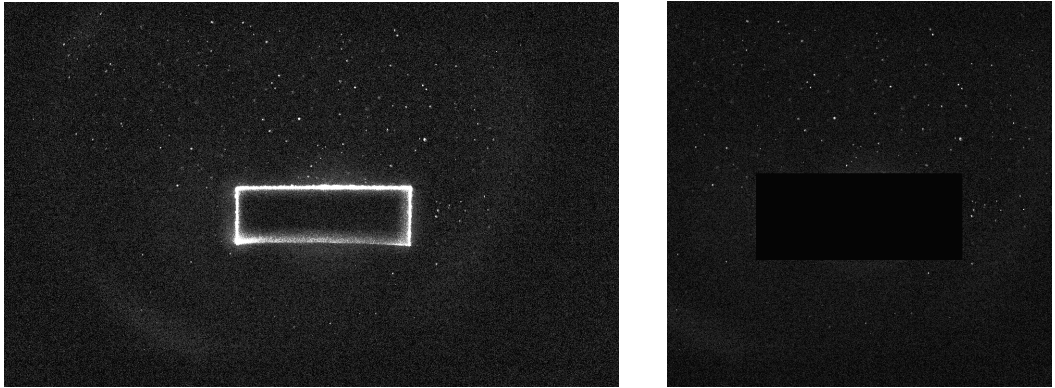
Figure 2.7: *Left:* Unprocessed, 1 Mpix frame captured by the camera. *Right:* The same frame, but cropped to 800×800 px and with the cylinder masked.

Firstly, the videos were processed by a custom-made software that was developed by Duda [20]. All the frames were cropped to 800×600 px or 800×800 px, in such a way that the cylinder is centered and the edges of the cryostat windows are no longer visible. Then, a dynamic rectangular mask was applied, so that it covers the proximity of the cylinder, due to parasitic light dispersion on the cylinder edges. After that, some color adjustments were done in order to reduce noise and to increase the contrast. Finally, the videos were stored as a sequence of grayscale (8-bit) `tiff` files.

Secondly, the files were loaded to the freeware tracking software ImageJ with Mosaic plugin installed [21]. After additional brightness and color adjustments, the software ran a particle detection routine, followed by a trajectory-linking routine. Hence, the output of this software was an `xls` file containting the positions of the particles with respect to time.

Thirdly, the ImageJ output files were loaded to another sofware developed by Duda [20]. This software is capable of esthablishing the velocity of all the particles calculated as the particle position difference between the n-th and $(n + 1)$-th frames, divided by the corresponding time shift between the frames (equal to the inverse frame rate). In addition, the software allows the use of various filters, e.g., of the total number of particles, minimum trajectory length and other relevant parameters.

As the motion of the cylinder is periodic, we can assume that the caracteristics of the flow induced by the cylinder are periodic too. Therefore, one can perform the *phase averaging*: the data corresponding to the same phase $\varphi = \omega t$ of the

cylinder oscillations are collected together. This procedudre, in theory, multiplies the number of trajectories by the number of periods performed by the cylinder in one run.

Then, the field of view is covered with a rectangular mesh of density to be specified later. For every mesh vertex point, we calculate a scalar quantity that can be linked with the vorticity, called the *theta parameter*, defined as

$$\theta(\mathbf{r}, \varphi) = \left\langle \frac{(\mathbf{r}_i - \mathbf{r}) \times \mathbf{v}_i}{|\mathbf{r}_i - \mathbf{r}|^2} \right\rangle_{|\mathbf{r}_i - \mathbf{r}| \leq R_{\max}, \, |\varphi_i - \varphi| \leq \Phi} \tag{2.3}$$

where $\mathbf{r}$ is the position of the mesh vertex, $\mathbf{r}_i$ denotes the position of the i-th particle and $\mathbf{v}_i$ indicates the particle velocity. The mean value is calculated from the set of the particles that are closer to a certain mesh vertex than the distance $R_{\max}$ and can be found in the phase window of width Φ.

Note that, the scaling of the θ parameter with $1/|\mathbf{r}_i - \mathbf{r}|^2$ compensates the scaling of the amount of included points and the scaling of the vector product with Φ and $R_{\max}$.

3   Results

The investigation of the flow generated by an oscillating rectangular cylinder was carried out both in He I and He II, for temperatures ranging from $3.0\,\mathrm{K}$ down to $1.2\,\mathrm{K}$. As mentioned above, the flow was driven by the motion of a small plexiglass cylinder of rectangular cross section, oscillating at various frequencies, from $0.05\,\mathrm{Hz}$ up to $1.25\,\mathrm{Hz}$, while two amplitudes of oscillation, $5\,\mathrm{mm}$ and $10\,\mathrm{mm}$, were used.

The conditions in the inner volume of the cryostat, i.e., temperature and pressure, were measured and stored using a purpose-made control unit written within the National Instruments LabView environment. With this unit the seeding system, described above, was controlled as well. The system provided the desirable amount of deuterium particles by injecting the mixture of D_2 and He gas, with the mass ratio of $1:100$, into the helium bath in a series of short pulses. Then, the motor connected to the cylinder via a long shaft was turned on, in order to damp the flow generated by the injection and to establish the periodic flow pattern. Approximately 45 seconds later, the data acqusition started: for each run, a video of $2\,000$ frames, at $100\,\mathrm{Hz}$ frame rate, was captured and saved.

The output of the experiment – 40 successful runs with $5\,\mathrm{mm}$ amplitude and 57 runs with the amplitude of $10\,\mathrm{mm}$ – was processed. In order to obtain the θ parameter defined above, we covered the processed field of view, i.e., $800\times600\,\mathrm{px}$ for $5\,\mathrm{mm}$ oscillation amplitude, and $800\times800\,\mathrm{px}$, for $10\,\mathrm{mm}$ amplitude, with meshes of 80×60 points and 80×80 points, for $5\,\mathrm{mm}$ and $10\,\mathrm{mm}$ amplitude, respectively. It was found that these mesh sizes are adequate for our purposes (see Discussion for more detail on the topic). Remaining parameters defining the θ parameter were chosen accordingly to be $R_{\max}=200\,\mathrm{px}$ and $\Phi=15°$.

The plots of the θ parameter show, in a well-defined manner, that this quantity maps the "strength" of the flow, see, e.g., fig. 3.1. One can notice the formation of two opposite vortex pairs in the proximity of the cylinder, within one period.

In addition, it is apparent that the shape and size of the vortices, visualised by θ, is roughly similar in both He I and in He II. Although here the images look similar, generally, the quality of the mapping in He I seems to be worse compared to that in He II, i.e., the vortices are less apparent in He I. This observation is also supported by the calculation of the relevant standard deviation, see fig. 3.3.
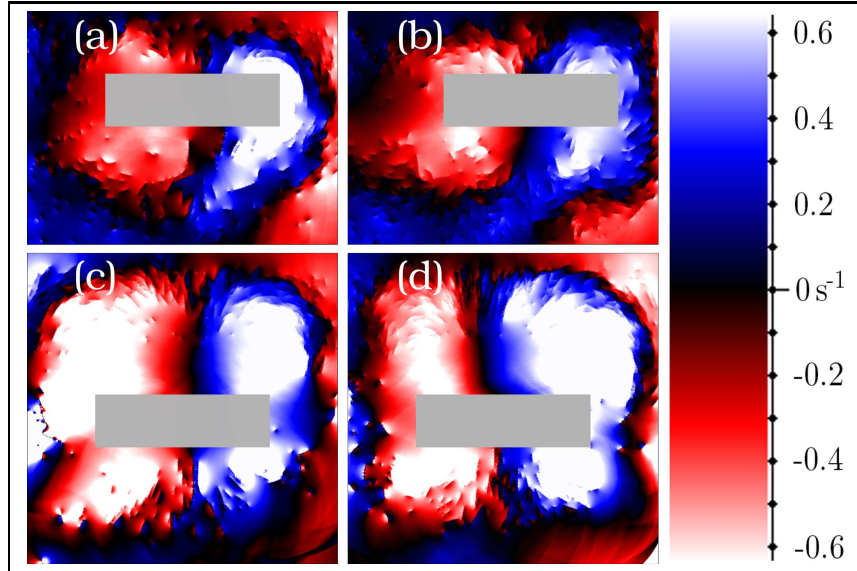
Figure 3.1: The map of the θ parameter, with mesh density of $800 \times 600\,\text{px}$, for (a) $5\,\text{mm}$ amplitude, at $2.18\,\text{K}$ (He I), (b) $5\,\text{mm}$ amplitude, at $1.35\,\text{K}$ (He II); and with mesh density of $800 \times 800\,\text{px}$, for (c) $10\,\text{mm}$ amplitude, at $2.17\,\text{K}$ (He I) and (d) $10\,\text{mm}$ amplitude, at $1.95\,\text{K}$ (He II). For all the cases, the frequency of oscillations was $0.5\,\text{Hz}$, the phase of points taken into account was $330° \pm 15°$. The gray rectangle depicts the position of the masked area. Note that, at this phase, the cylinder moves upwards, after having reached, at $270°$, the lowest position of the cycle.

However, the map of our parameter does not allow the straightforward comparison between various flow conditions. Hence we decided to characterize each run with one quantity only, that was chosen to be *the averaged theta squared parameter*, $\langle \theta^2 \rangle$. The averaging was executed through all the points of the mesh and then through all the phases of one period: the evaluation of θ was carried out at phases ranging from $0°$ to $360°$, with $2\Phi = 15°$ step. Hence, 40 data sets, including all the points detected in one run, were calculated and averaged. $\langle \theta^2 \rangle$ can be naively understood as "the magnitude" of the vortex structures.

## 3.1   Definition of Relevant Reynolds Number

As the experimental setup remained the same during the experiment, it is safe to state that, for the same boundary conditions of the flow, i.e., the size of the optical tail and the cylinder dimensions, different data sets can be compared, each to another, if we use the Reynolds number, defined as the product of Keulegan-Carpenter number KC (1.15) and Stokes number β (1.16). Note that β is inversely proportional to the viscosity of the fluid.

Kinematic viscosity of He I is well-known an tabulated [22], while a correct definition of kinematic viscosity of He II in mechanically driven flows remains a question that is yet to be answered. Hereby we employ a single model proposed by L'vov et al. [23]. This model suggests that the viscosity of liquid helium is, in proximity of the lambda transition, a smooth function of temperature. Hence, one can derive that the viscosity of He II, at temperatures close to the transition, equals approximately to $\kappa/6$. In the simplest case, one can assume that the viscosity of He II does not change rapidly within our temperature range. Therefore, we can set for the kinematic viscosity of He II a constant value of $\kappa/6$ for the whole temperature range.

The results, i.e., a plot of $\langle \theta^2 \rangle$ as function of the Reynolds number defined above is shown in fig. 3.2.

At the first sight, one can notice that data taken in He II collide in a few discrete lines, with different values of $\langle \theta^2 \rangle$. The reason is as follows: κ is a physical constant ($\kappa = h/m_4$), hence the values of the Reynolds number for He II data depend, beside constant parameters, only on discrete values of frequency and amplitude of cylinder oscillations.

Furthermore, we can observe that the data taken in He II (blue circles) collide into a line that increases with the Reynolds number (note that the figure 3.2 is in log-log scale). Interestingly, it seems that data in He I collide in a curve as well, but their scatter is significantly larger. In order to obtain a relevant and robust conclusion from our data, additional studies on data quality were carried out, see below.
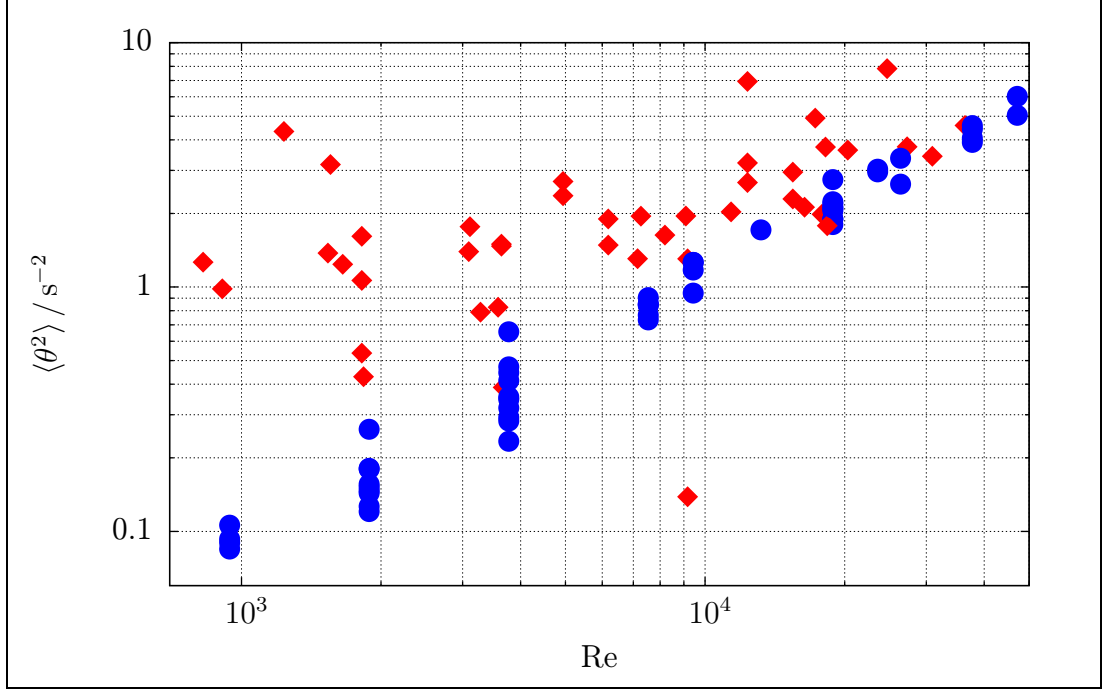
Figure 3.2: Plot of $\langle \theta^2 \rangle$ parameter as function of Reynolds number Re defined above. Here and below, full red diamonds denote data taken in He I, i.e., a viscous fluid, while full blue circles represent data taken in He II, i.e., a superfluid. Only trajectories longer than 5 points are included.

3.2 Study of the Data Scattering

Due to scattered data in fig. 3.2 it is useful to investigate the incertitude in the calculation of our parameter in more detail. For each value of θ^2, corresponding to a specific point of the mesh and a specific phase interval, we evaluated the standard deviation as

$$\sigma_{\theta^2} = \sqrt{\frac{1}{N}\left[\sum_{i=1}^{N}\theta_i^2 - \left(\sum_{i=1}^{N}\theta_i\right)^2\right]}, \tag{3.1}$$

where N is the total number of points taken into account when evaluating θ^2. Then, in order to obtain the standard deviation of $\langle\theta^2\rangle$, we proceeded with an analogue averaging routine, i.e., we calculated the mean value through all the mesh points and all the phases.

The values of the $\langle\theta^2\rangle$ parameter in linear scale and their relative errors, defined as $\delta = \langle\sigma_{\theta^2}^2\rangle / \langle\theta^2\rangle$, are plotted in fig.3.3.

26
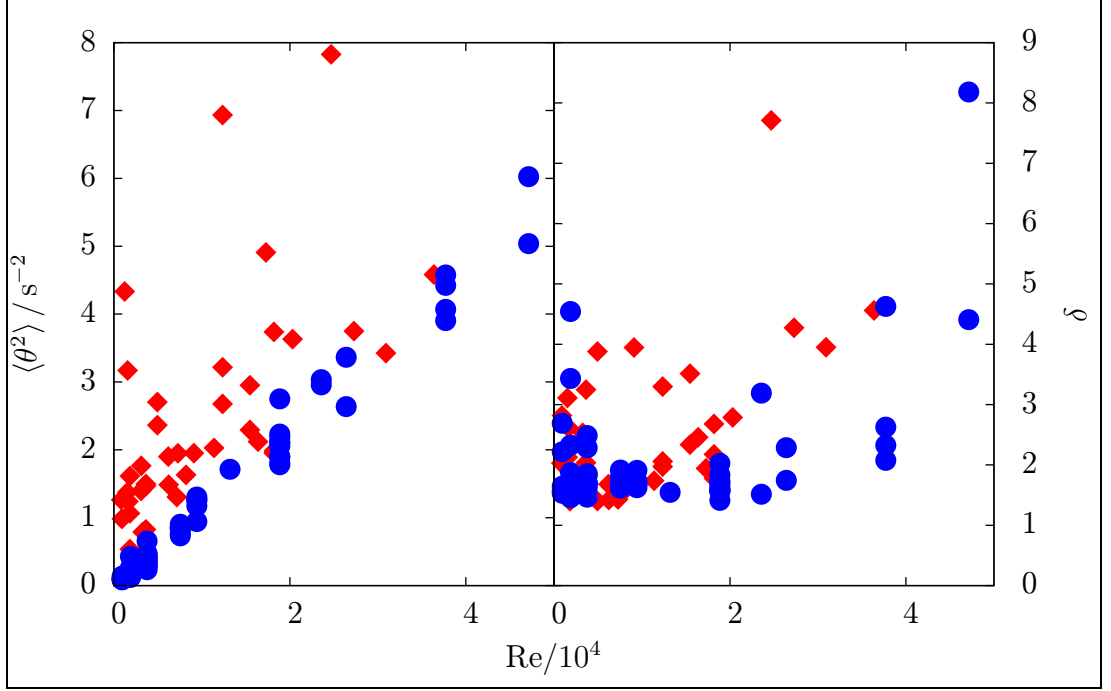
Figure 3.3: For notation, see fig. 3.2 above. *Left:* Linear plot of $\langle\theta^2\rangle$ as a funcion of Re. Note that the overall shift in values of $\langle\theta^2\rangle$ between the two phases of liquid helium is visible also in linear scale. *Right:* Plot of δ as a funcion of Re.

The figure clearly shows that the standard deviation is, for all the cases, greater than the value of the parameter itself, i.e., $\delta > 1$. Statistical scattering of the data cannot be thus neglected. We can observe that, for measurements in He II, the relative error for a majority of the cases is roughly constant, at $\delta \approx 2$. On the contrary, the relative errors in viscous He I display a larger data scattering, ranging from 1.5 to 8.

Same data points exhibit, however, a greater relative error than the constant trendline of the data set indicates. It is possible that, for these measurements, the conditions in the cryostat might have been unfavourable, e.g., a small amount of particles was dispersed in the field of view, residual flows from the particle injection were present, etc. Therefore, the data set was filtered in order to enhance its quality and to reduce the average relative error.

3.3   Filtering of the Data

Total Amount of Particles

A common issue we noticed when processing the raw data was an occasional lack of particles in the field of view, resulting in considerably smaller total amount of detected particles. It is hence possible that these runs display a large value of the error due to a poor statistics. In order to improve the statistics of the whole data set, for the following plots, we excluded all the runs whose total number of detected particles is smaller than 35 000. In effect, this procedure reduced the total number of suitable runs by approximately 30%, but, at the same time, reduced the mean relative error.

Same Re Averaging

Due to the fact that some data points belong to the same value of Re, one can easily calculate the mean values and standard deviations of such data subsets. This procedure noticeably simplified the data and led to the decrease of δ as well.

The results of the two filters are shown in fig. 3.4.

Minimal Trajectory Length

As mentioned above, our field of view consisted of a sharply focused plane. However, as the flow in the experimental tail is tridimensional, the particles often tend to leave the focused plane, rendering their trajectories, in the plane of the field of view, discontinuous or very short. However, in order to reduce the error, it is possible to pick the trajectories longer than some treshold value. Note that this procedure has been already done in previous figures, whereas the treshold length was set to be 5 points.

In this study, we restricted ourselves to trajectories longer than 20 points. However, this filtering turned out to bee too strict. The procedure led to a small decrease of the error, but to a serious loss of statistics. Contrarily, the decrease of the treshold value did not reduce the error significantly. Hence the additional filtering on the minimum trajectory length appeared to be ineffective.
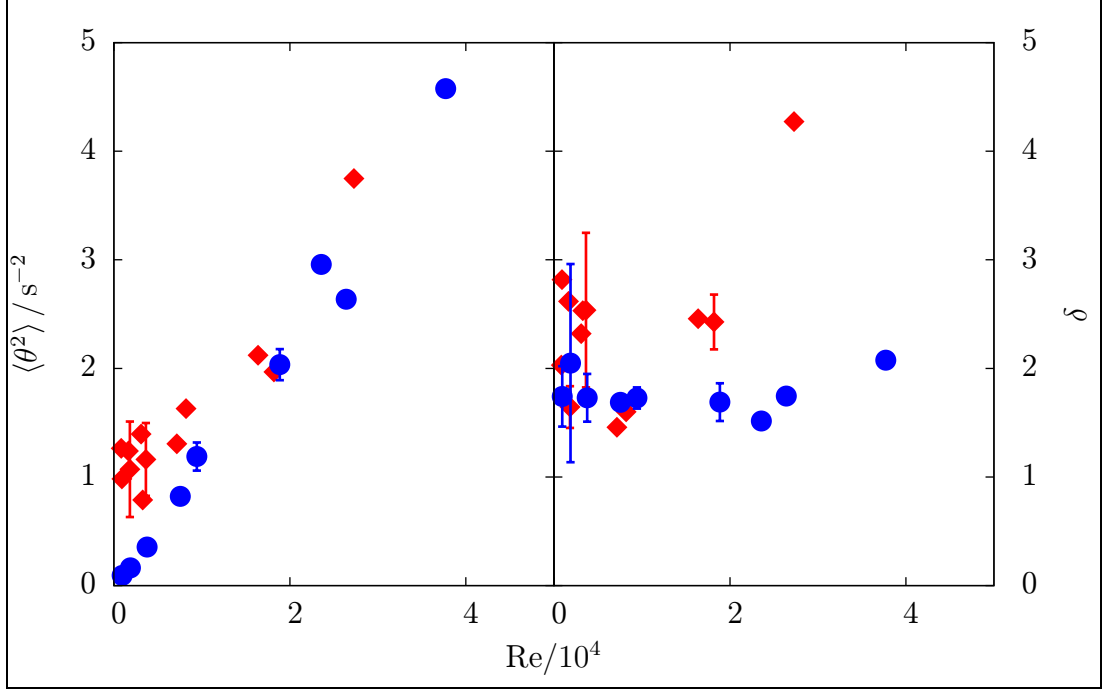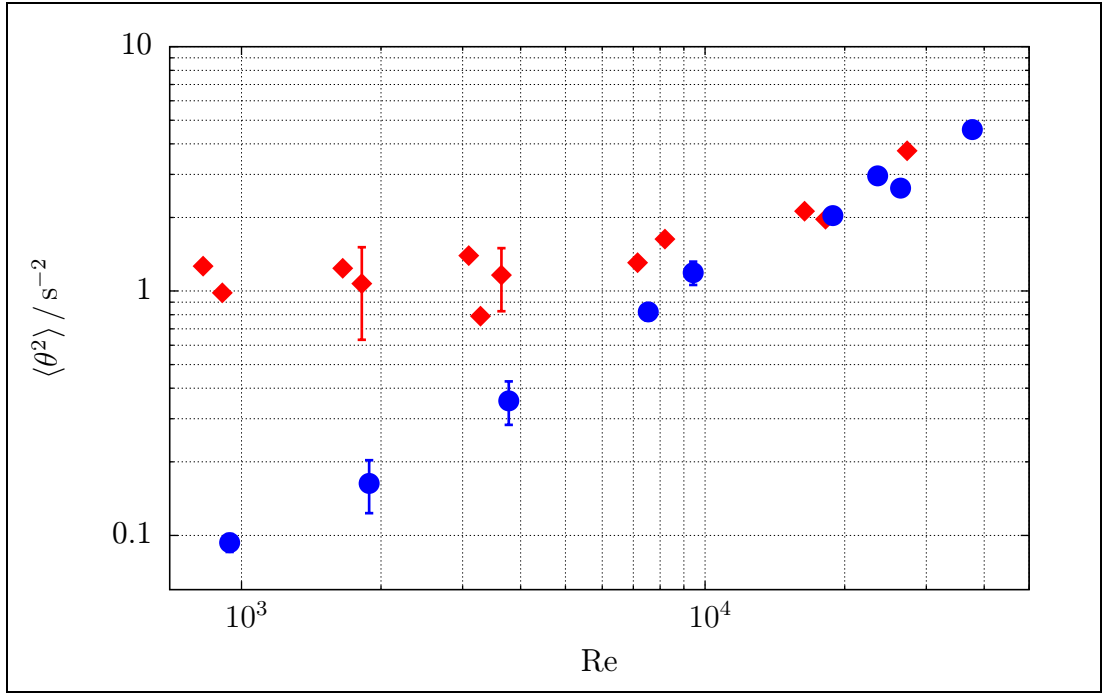
Figure 3.4: For notation, see fig. 3.2 above. *Left:* Plot of $\langle\theta^2\rangle$ as a function of Re. The data consist of events with more than $35\,000$ detected particles; data taken at the same value of Re were averaged. Errorbars denote the standard deviation of such data points. *Right:* Plot of the relative error δ of the filtered data as function of Re.

3.4   Summary

In our experiment, a careful study of the macroscopic vortex structures was carried out, in He I and in He II, using the particle tracking velocimetry technique. The flow in the helium bath was driven by the motion of a small cylinder of rectangular cross-section, oscillating with tunable frequency and amplitude.

In order to characterize the observed flow patterns in the liquid, we introduced a dimensionless parameter, the Reynolds number, similar to that used for classical viscous flows and we justified its use in our superfluid experiments as well.

A study on the motion of tracer particles was performed, resulting into the use of the $\langle\theta^2\rangle$ parameter as the quantity that represents the "strength" of present vortex structures. After a noise-reducing procedure, a final function of this parameter was obtained, see fig. 3.5. One can clearly see that the data collapse into two different curves, which can be linked to the normal and superfluid phases. However, keep in mind that the data are still burdened with an error larger than the measured value.

Figure 3.5: Plot of $\langle \theta^2 \rangle$ as a function of Re, including only points that passed all the filters applied. For notation, see fig. 3.2 above.

To support our findings, a few questions are yet to be discussed: is $\langle \theta^2 \rangle$ a well-defined and suitable parameter? Is there the possibility of a trivial reason for the two-way behavior or it is possible, in some way, to explain the results generally?

4 Discussion

4.1 Convergence Study

Investigating the robustness of the used data processing approach, especially the relevance of the $\langle \theta^2 \rangle$ parameter, is necessary in order to obtain results that are, in a broad sense, independent on the choice of parameters. Hence, a detailed study, focusing on the behavior of the free parameters that are used in the evaluation of $\langle \theta^2 \rangle$, was carried out.

For the purposes of the study, we selected two measurements:

1. cylinder amplitude of $10\,\mathrm{mm}$ and frequency of $0.5\,\mathrm{Hz}$, at $1.94\,\mathrm{K}$ and $\mathrm{Re} \approx 3.3 \times 10^4$; the field of view was $800 \times 600\,\mathrm{px}$,

2. cylinder amplitude of $5\,\mathrm{mm}$ and frequency of $0.5\,\mathrm{Hz}$, at $1.23\,\mathrm{K}$ and $\mathrm{Re} \approx 1.2 \times 10^4$; the field of view was $800 \times 800\,\mathrm{px}$.

Influence of the Mesh Density

For both data sets, we evaluated the $\langle \theta^2 \rangle$ parameter for various mesh densities, from 4×3 to 400×300 points, for the first one, and from 30×30 up to 300×300 points, for the second one. Other parameters were kept constant: $R_{\mathrm{max}} = 200\,\mathrm{px}$ and $\Phi = 15°$.

In figure 4.1, one can observe that, for both cases, the value of $\langle \theta^2 \rangle$ converges quickly for the meshes containing more than $5\,000$ points. Hence, the optimal mesh density is such that the calculation consumes the smallest computing time, but provides sufficient spatial resolution. Hence, for the data processing, we chose the mesh containing 80×60 and 80×80 points, i.e., $4\,800$ and $6\,400$ points in total, for the fist and the second case, respectively.
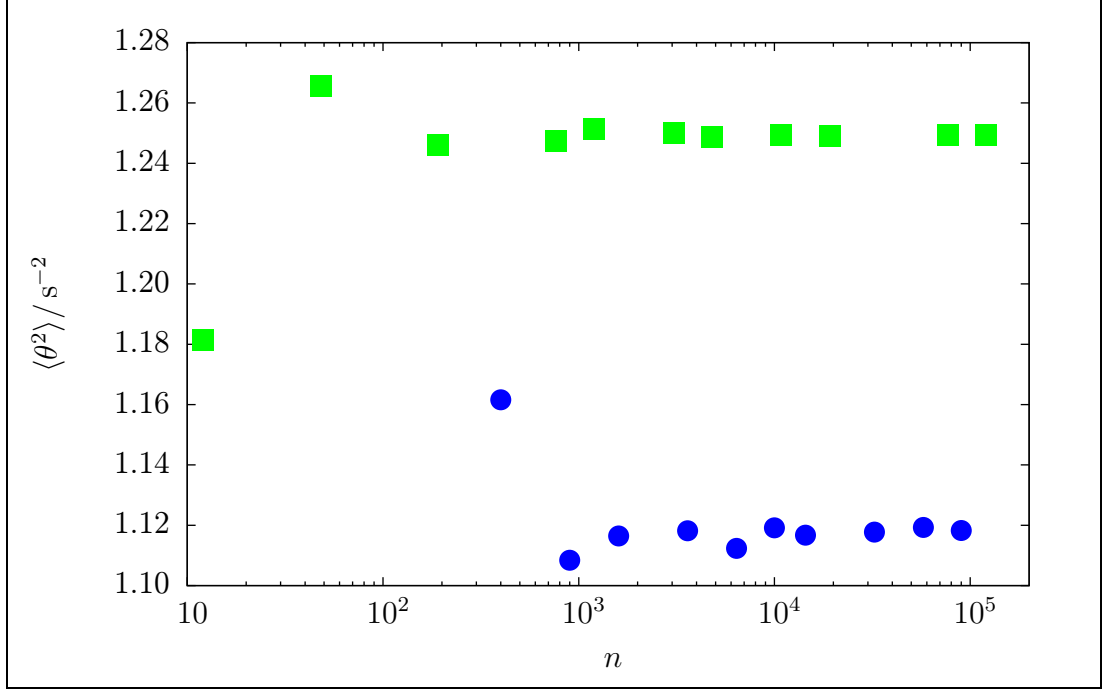
Figure 4.1: Dependence of the $\langle\theta^2\rangle$ parameter on the mesh density, here characterised by the total amount of mesh points n. Green squares represent the first run (10 mm amplitude), blue circles indicate the second run (5 mm amplitude).
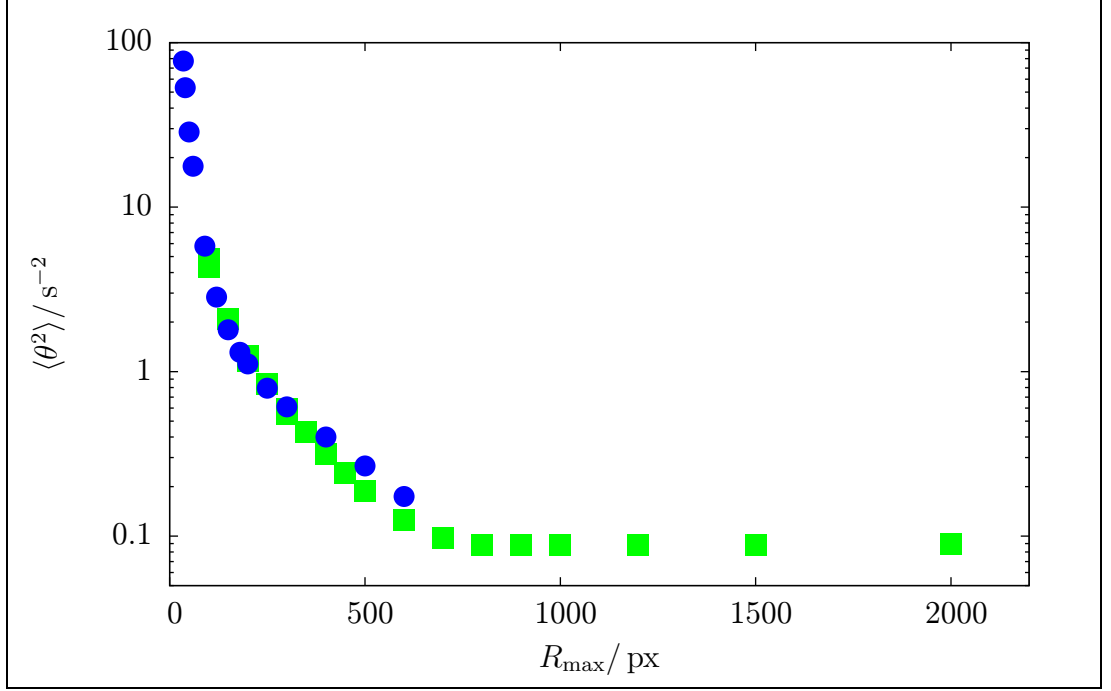
Influence of R$_{\text{max}}$

This parameter determines the maximum distance, for each mesh point, from which the points contribute to the value of θ. Figure 4.2 shows that, for both measurements, the value of $\langle\theta^2\rangle$ decreases as R_{max} increases. This behavior can be explained if we take into account that, besides big vortices, apparent in the map of the θ parameter (see fig. 3.1), the regions close to the edges of the field of view are mostly noisy areas with no distiguishable flow patterns.

In addition, for the field of view of 800×600 px, the value of

$$R_{\text{max}} = \sqrt{800^2 + 600^2} \, \text{px} = 1000 \, \text{px}$$

covers, for each point of the mesh, all the points in the field of view. Hence, for $R_{\text{max}} > 1000$ px, the value of $\langle\theta^2\rangle$ must remain constant (as it is evident from the figure). The critical radius, for the mesh of 800×800 px, is $R_{\text{max}} \approx 1130$ px.

However, the use of such a big radius of interest does not have any physical meaning, as we are dealing with two vortices of diameter about 200 px. This value was therefore chosen to be the default value for the computation of our parameter.

Figure 4.2: Parameter $\langle\theta^2\rangle$ as a funcion of $R_{\max}$. Symbols as in figure 4.1.

Influence of Φ

The dependence of our parameter on the choice of Φ is presented here only for the second case, as the results obtained for the first measurement are qualitatively equivalent.

We evaluated the $\langle\theta^2\rangle$ parameter, for various values of Φ, ranging from $5°$ to $30°$, see figure 4.3. In addition, we plotted, for each value of Φ, the total amount of points used in the evaluation of the parameter.

One can clearly observe the decrease of $\langle\theta^2\rangle$ as Φ increases. For increasing Φ, a bigger portion of the period of oscillations in taken into account. Therefore, the correlation between the motion of tracer particles is less apparent, which leads to the decrease of the parameter, as observed. In addition, the function of the total amount of particles, that is rougly linear, indicates that the particle density is approximately constant.

The choice of the suitable value of Φ must consequently meet two opposite criteria: the phase window must be narrow enough, so that the motion of the particles does not change significantly and, additionally, the total number of particles taken into account should provide reasonable statistics. For our purposes, the ideal width appeared to be $\Phi = 15°$, i.e., for one value of the phase ϕ, the averaging goes

through the interval of $\phi \pm 7.5°$. This choice provides the typical statistics of approximately 3 000 points, dispersed in the field of view.
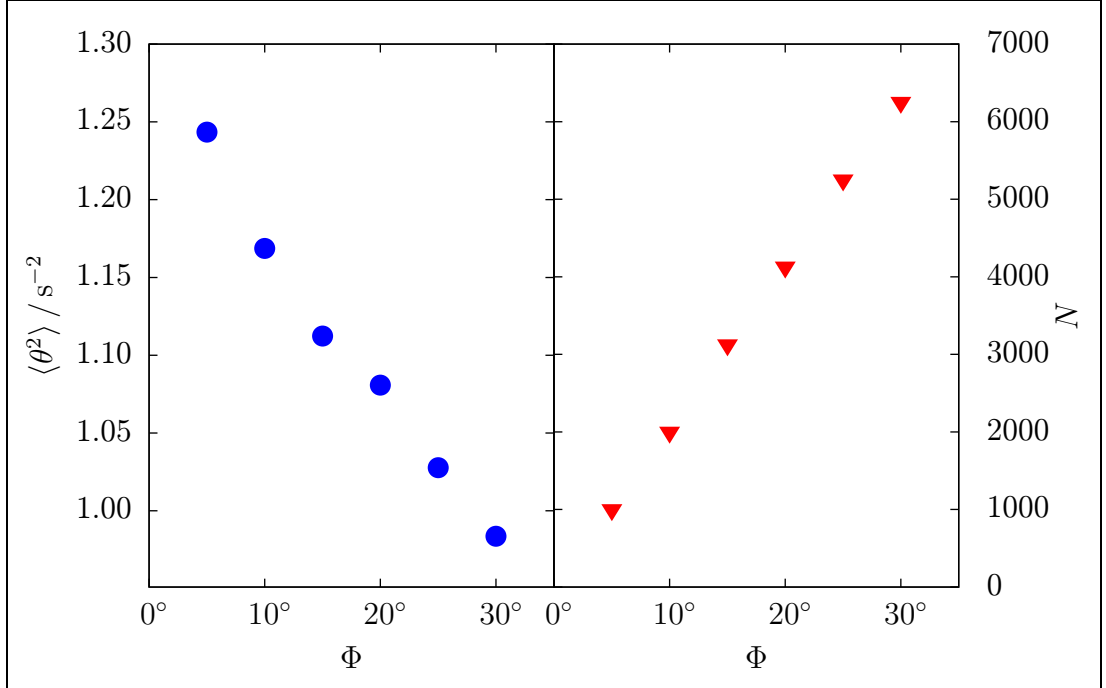
Figure 4.3: *Left:* Dependence of $\langle \theta^2 \rangle$ on Φ. *Right:* Plot of the total number of points in the field of view, N, meeting the phase restriction.

4.2   Interpretation of the Data

Finite spatial resolution of our setup and final size of our probes, i.e., the particles, limit the length scales we can access to. For our experiment, the *probed length scale*, δ, can be accordingly defined as the minimal displacement of the particles between the two consecutive frames.

For the frame rate φ, one obtains $\delta \approx v_{\mathrm{particles}}/\varphi$. Additionally, we can replace $v_{\mathrm{particles}} \approx v_{\mathrm{cylinder}}$, as these velocities were observed to be of the same order. Hence we get

$$\delta \approx \frac{v_{\mathrm{cylinder}}}{\varphi} = \frac{2\pi f a}{\varphi}. \tag{4.1}$$

Other relevant length scales result form the hydromechanical properties of viscous He I and superfluid He II. Characteristic length scale of He II flows, called the *quantum length scale*, l_{Q}, is the intervortex distance, i.e., the mean distance between two quantized vortices. This quantity can be estimated if we consider that the vorticity of the superfluid component can be written as $\omega_{\mathrm{s}} = \kappa L$, where κ

is the quantum of circulation and L denotes the density of the vortex lines (total length of vortex lines per unit volume). The latter can be expressed as $L = 1/l_{\mathrm{Q}}^2$.

The net vorticity of the liquid in coflow, ω, can be linked to ω_{s} via the ratio of the normal and superfluid components: $\omega \approx \omega_{\mathrm{s}} \varrho / \varrho_{\mathrm{s}}$. An estimate of the vorticity can be done if we identify $\omega^2 \approx \langle \theta^2 \rangle$.

Hence the mean intervortex distance, or the quantum length scale can be expressed as

$$l_{\mathrm{Q}} = \frac{\sqrt{\kappa \varrho / \varrho_{\mathrm{s}}}}{\sqrt[4]{\langle \theta^2 \rangle}}. \tag{4.2}$$

In the case of viscous flows of He I, characteristic length scale is the *Kolmogorov length scale*, l_{K}. This length scale limits the existence of coherent vortex structures, because viscous vortices of diameter of the order of l_{K} quickly decay and their kinetic energy is dissipated into heat. Kolmogorov length scale is defined [11] as

$$l_{\mathrm{K}} = \sqrt[4]{\frac{\nu^2}{\omega^2}} = \sqrt[4]{\frac{\nu^2}{\langle \theta^2 \rangle}}. \tag{4.3}$$

Note that in the equation above we used again that $\omega^2 \approx \langle \theta^2 \rangle$.

Finally, we can define the ratio between the probed and hydrodynamical length scales, ℓ as

$$\ell = \frac{\delta}{l}, \tag{4.4}$$

where $l = l_{\mathrm{K}}$ for He I and $l = l_{\mathrm{Q}}$ for He II.

Plot of ℓ as function of Re shows fig. 4.4. The fact that ℓ increases with Re can be assigned to either increasing mean velocity of the particles, i.e., increasing δ or decreasing l_{Q} and l_{K}.

At $\mathrm{Re}_{\mathrm{c}} \simeq 10^4$, we get $\ell \simeq 1$, for both He I and He II data. In other words, for $\mathrm{Re} < \mathrm{Re}_{\mathrm{c}}$ the probed length scale δ is *smaller* than l_{K} and l_{Q}.

Surprisingly, the same value of Re_{c} splits one-line and two-line behavior of $\langle \theta^2 \rangle$ as function of Re (see fig. 3.5). We believe that such a correlation, that was not observed before, is based on the underlying physics of quantum and classical hydromechanics.

We thus suggest an explanation of this phenomenon: for $\mathrm{Re} < \mathrm{Re}_{\mathrm{c}}$, flows of He I are no longer coherent due to viscous dissipation at the Kolmogorov length scale. However, flows of He II, at length scales smaller than l_{Q}, remain coherent

due to quantized vortices whose size is much smaller than their mean intervortex distance.

Contrarily, for Re > Re$_c$, the probed length scale is greater than l_Q, i.e., in He II, we can only probe the behavior of multiple quantized vortices at once. The collapse of two lines in fig. 3.5 into one hence indicates that the macroscopic behavior of quantizes vortices does mimic viscous-like flows, observed in He I, at the same Reynolds number.
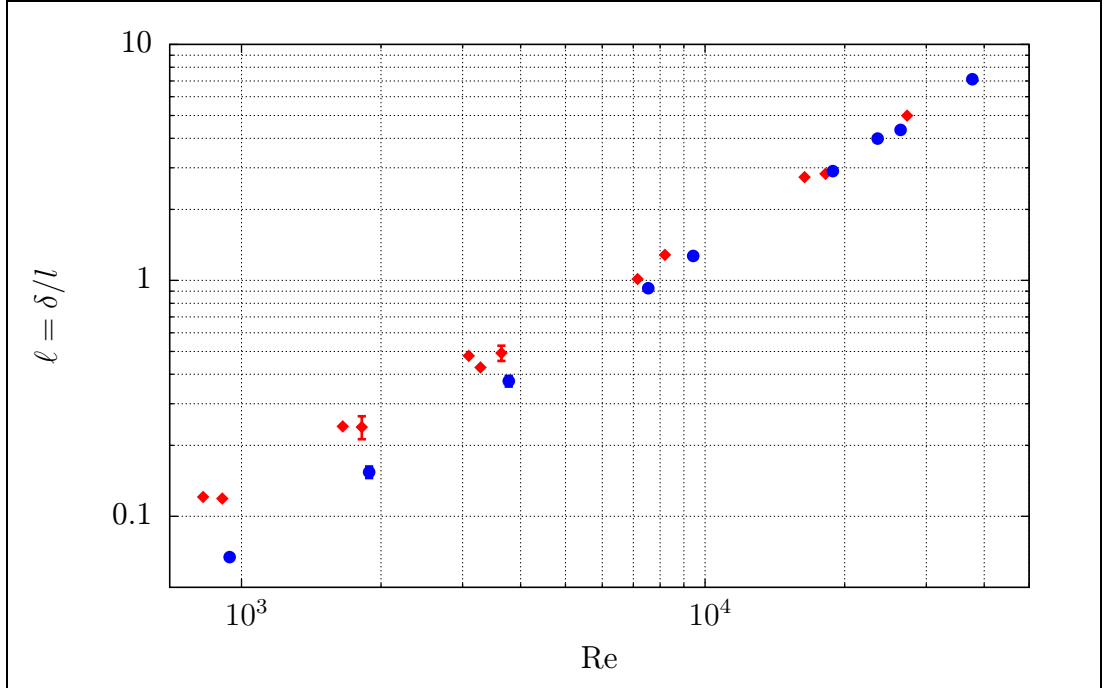
Figure 4.4: Plot of ℓ, i.e., the ratio between the probed length scale δ and the intervortex distance l_Q or the Kolmogorov length scale l_K, for He II and He I, respectively (see text for relevant definitions). Data points and their errorbars represent the same runs as in fig. 3.5.

Furthermore, we cannot neglect the heat input into the experimental volume due to both the laser and the oscillating cylinder. Although the power input, of the order of a few miliwatts, was roughly constant for all the runs, heat conductivities of He I and He II differ by a factor of ca. 10^6. Such a difference may affect the heat transfer and dissipation in He I and He II and provide additional effects (such as parasitic large scale flows) and modify our results.

5   Conclusion

The study of the behavior of macroscopic vortex structures, generated by an oscillating sharp-edged body, was carried out using flow visualisation techniques. A small rectangular cylinder ($3 \times 10 \, \mathrm{mm}^2$ cross section), submerged in a liquid helium bath, performed quasi-harmonic oscillations at various frequencies ($0.05 \, \mathrm{Hz}$ – $1.25 \, \mathrm{Hz}$) and amplitudes ($5 \, \mathrm{mm}$ and $10 \, \mathrm{mm}$), at different temperatures ($1.2 \, \mathrm{K}$ – $4.0 \, \mathrm{K}$). Thus, in our experiment, a direct comparison between similar mechanically driven flows in He I, a viscous Newtonian fluid, and He II, a liquid displaying superfluidity, was carried out.

Each measurement was, for this comparison, quantified by a custom-defined θ parameter, see equation (2.3). For the first time, it was observed both qualitative and quantitative differences between He I and He II macroscopic flows. The results, after careful study of the quality of the data set and the robustness of the method, displayed that the values of $\langle \theta^2 \rangle$, taken in He I, are about 10 times larger than in He II, for $\mathrm{Re} \lesssim 10^4$. For values of $\mathrm{Re} \gtrsim 10^4$, this effect vanishes – both liquids, i.e., He I and He II, appear to behave similarly.

We found that the value of $\mathrm{Re} \simeq 10^4$ is represents also a value at which the probed length scale reaches the Kolmogorov length scale, i.e., in He I, coherent vortex structures cease to exist due to finite viscosity of the fluid. However, He II flows remains present due to quantized vortices whose presence in He II results from the laws of quantum mechanics having no classical analogue.

Keep in mind, however that the obtained numerical values are affected by the data scattering, which was found to be, for the averaged parameter $\langle \theta^2 \rangle$, about two times larger than the measured quantities. In other words, the results presented here can be mostly regarded as qualitative ones giving however meaningful physical insight into the investigated problem.

The study of periodic flows of liquid helium, especially close to the flow source

should be carried out in more detail. It is, for example, yet to investigate how the sharp edges of the body influence the formation of macroscopic vortices in He II and whether this behavior is consistent with the results obtained in classical fluids [17]. In addition, more precise investigations, carried out, for example, by using a faster camera, should be perfomed, in order to study the flow at higher frequencies. It is also expected that cavitation, i.e., formation of small bubbles in the liquid volume, wolud occur in the proximity of the edges, also in He II. This phenomenon, already reported by researchers, is yet to be understood in detail, rendering it a vivid field of research in modern fluid mechanics.

Bibliography

[1] DUDA D. et al. *Phys. Rev. B* **92**, 064519 (2015)

[2] SKRBEK L. et al. *Fyzika nízkých teplot.* 1. vydání. Praha: *MatfyzPress*, 2011. ISBN 978-80-7378-168-2.

[3] DONELLY R. J. and BARENGHI C. F *J. Phys. Chem. Ref. Data* **27**, 1217 (1998).

[4] SKRBEK L., SREENIVASAN K. R. *Phys. Fluids* **24**, 011301 (2012).

[5] GUO W. et al. *PNAS* **111**, 4653 (2014).

[6] KAPITSA P. *Nature* **141**, 74 (1938).

[7] ALLEN J. F., JONES H. *Nature* **141**, 243 (1938).

[8] TISZA L. *Nature* **141**, 913 (1938).

[9] LANDAU L. D. *J. Phys. USSR* **5**, 536 (1941).

[10] ANDRONIKASHVILI E. L. *Journal of Physics* **10**, 201 (1946).

[11] LANDAU L. D., LIFSHITZ E. M. *Fluid Mechanics.* Second English Edition. *Pergamon Books Ltd.*, 1987. ISBN 0-08-033933-6.

[12] LA MANTIA M., SKRBEK L. *EPL* **105**, 46002 (2014).

[13] CHARALAMBOUS D. et al. *J. Low Temp. Phys.* **145**, 107 (2006).

[14] KEULEGAN G. H., CARPENTER L. H. *J. Res. Natl. Stand.* **60**, 423 (1958).

[15] SCHMORANZER D. et al. *Phys. Rev.* **81**, 066316 (2010).

[16] VINEN W. F., SKRBEK L. *PNAS* **111**, 4699 (2014).

[17] TAO L., THIAGARAJAN K. *Appl. Ocean Res.* **25**, 21 (2003).

[18] La Mantia M. et al. *Rev. Sci. Instrum.* **83**, 055109 (2012).

[19] Duda D. et al. *J. Low Temp. Phys.* **175**, 331 (2014).

[20] Duda D. et al. *Proceedings of the 2014 Week of the Doctoral Students*, 73 (2014).

[21] Sbalzarini I. F., Koumoutsakos P. *J. Sctruct. Biol.* **151**, 182 (2005).

[22] Arp V. D., McCarty R. D. The properties of critical helium gas. *Technical Report, University of Oregon, Eugene, USA* (1998)

[23] L'vov V. et al. *Phys. Fluids* **26**, 041703 (2014).